J. Plasma Phys. (2016), *vol.* 82, 615820202
doi:10.1017/S0022377816000404

Existing and new applications of micropellet injection (MPI) in magnetic fusion

Zhehui Wang[1],†, Robert Lunsford[2], Dennis K. Mansfield[2] and Jacob H. Nichols[2]

[1]Los Alamos National Laboratory, Los Alamos, NM 87545, USA

[2]Princeton Plasma Physics Laboratory, Princeton, NJ 08544, USA

(Received 1 February 2016; revised 31 March 2016; accepted 1 April 2016)

The intense heat and energetic particle fluxes expected in ITER and future magnetic fusion reactors pose prohibitive problems to the design, selection and maintenance of the first wall and divertor. Micropellet injection (MPI) technologies can offer some innovative solutions to the material and extreme heat challenges. Basic physics of micropellet motion, ablation and interactions with high-temperature plasmas and energetic particles are presented first. We then discuss MPI technology options and applications. In addition to plasma diagnostic applications, controlled injection of micropellets of different sizes, velocities and injection frequencies will offer several possibilities: (1) better assessment of the core plasma cooling due to dust produced *in situ*; (2) better understanding of the plasma–material interaction physics near the wall; (3) new methods for plasma fuelling and impurity control; and (4) techniques for edge cooling with minimal impact on the plasma core. Dedicated small-scale laboratory experiments will complement major fusion experiments in development and applications of MPI.

1. Introduction

Practical fusion energy depends on resolutions of material issues arising from plasma–material interactions (PMIs) (Federici *et al.* 2001; Brooks 2002). The ITER fusion reactor has been designed to generate a steady fusion power of 500 MW and is expected to be the first magnetic fusion device with a fusion power gain factor (Q) of no less than 10. In steady-state operations, about 80 % or 400 MW of the fusion power will be carried by 14.1 MeV neutrons, which corresponds to a flux of 1.77×10^{20} s^{-1}, and they are emitted isotropically onto the first wall. Neutron flux may increase by a factor of 10 due to nuclear reactions within the wall (Behrisch 1991). An earlier version of the ITER first wall had a total surface area of 850 m^2: 700 m^2 of Be (main chamber), 100 m^2 of tungsten (W) (diverter) and 50 m^2 of C (divertor strike point). More recently, a full W divertor has been adopted for its first day of operation (Pitts *et al.* 2013). The steady neutron energy flux to the first wall is therefore less than 1 MW m^{-2} on average, while the engineering heat load limit is about 10 MW m^{-2}.

† Email address for correspondence: zwang@lanl.gov

Type	Energy release ($\times W_0$)[a]	Time scale (ms)	Frequency (Hz)
ELMs (type I)	2–6 %	0.1–1	1–2
VDEs	1–10 %	300	<1
Disruptions (thermal)	80–100 %	1–5	1.5–5 %[b]
Disruptions (RE current)	50–70 %[c]	50–150	1.5–5 %[b]

TABLE 1. A summary of major transient events in magnetic fusion.

[a]$W_0 \sim 350$ MJ is the total thermal plasma energy in ITER.
[b]Out of the total number of discharges.
[c]The plasma current corresponds to about 1 GJ of energy in ITER.

In comparison, the other 20 % or 100 MW of the power in steady operations will be carried by the α particles. The rest of the charged particle energy is channelled through the scrape-off layer (SOL) to the ITER divertor, which has a strike zone area of about 10 m^2. The steady-state heat-flux density is at least a factor of 10 higher to the divertor than to the first wall.

While the steady heat flux during normal operations of ITER can be handled by the plasma-facing components, transient heating due to natural edge-localized modes (ELMs), disruptions and vertical displacement events (VDEs) during H-mode operations could exceed the engineering limits and thus accelerate mass loss (Loarte *et al.* 2014). When 2–6 % of the stored thermal energy (~350 MJ in ITER) is released in a type-I ELM event within 0.1–1 ms, as summarized in table 1, the peak power density can exceed the ablation threshold by a factor of five (Leonard *et al.* 1999). Disruptions due to global plasma instabilities can result in a quick termination of the plasma and lead to even worse wall damage if not mitigated. Furthermore, while the divertor damage at smaller currents may be less significant, control of W migration from the divertor region to the core plasma in order to maintain its concentration below 10 parts per million (ppm), or about 0.25 mg, will still be needed.

Recent experimental successes of cryogenic pellet and lithium granule injection for heat mitigation motivate micropellet injection (MPI) technologies for heat mitigation in ITER-like conditions. Deuterium pellet injection has successfully induced ELMs at up to 12 times the natural frequencies in H-mode deuterium plasmas (Lang *et al.* 2004; Baylor *et al.* 2013). Lithium granule injection has also demonstrated near 100 % efficiency in inducing ELMs (Mansfield *et al.* 2013). For ITER, it has been proposed to induce ELMs at a frequency at least 30 times the natural ELM frequency (Lang *et al.* 2013), or 30–40 Hz. Shattered cryogenic pellet injection is also being developed for disruption mitigation in ITER.

One of the existing applications of MPI is an experimental study of dust dynamics, generation, motion and destruction. We first discuss dust motion under magnetic fusion-relevant conditions, and identify size and velocity requirements for MPI. We then discuss micropellet destruction physics separately, since this is essential to impurity generation due to dust ablation, diagnostics and heat mitigation. Another possible application of MPI is to mitigate effects of energetic particles, in particular runaway electrons during disruptions. Our discussions are based on analytical methods, which may not be enough to interpret dust phenomena in fusion devices in detail but sufficient to guide MPI development and experiments. In conclusion, many

https://doi.org/10.1017/S0022377816000404 Published online by Cambridge University Press

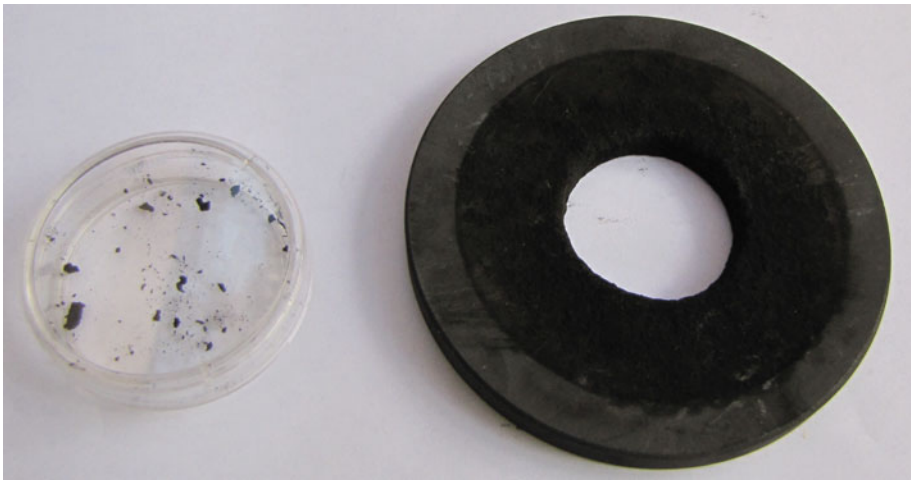

FIGURE 1. (Left) Dust of different sizes and irregular shapes collected from an arc discharge using graphite as the cathode and a mixture of hydrogen and argon. (Right) Another graphite electrode nearby shows redeposition of carbon.

opportunities exist for diversified MPI technologies in the ITER era. Efforts in major fusion facilities can be supplemented by smaller scale experiments in developing MPI.

2. Dust motion

Dust production cannot be avoided in ITER-like conditions and it is a part of PMI physics (Federici *et al.* 2001; Brooks 2002). The three primary concerns with PMI are (1) limiting lifetimes of plasma-facing components; (2) contamination of the core plasma due to transport of wall materials into the plasma; and (3) tritium buildup in the fusion device due to adsorption and redeposition of tritium on the wall during deuterium–tritium (DT) operations, an issue also known as tritium retention. *In situ*-produced dust can be a significant factor in all three aspects. To use MPI for dust physics and PMI studies, it is necessary to use micropellets of similar composition, sizes, structures and velocities.

2.1. *Dust sizes*

Dust-size distributions in fusion experiments are conveniently measured by collecting samples from the experiments. We show an example from a carbon-arc discharge here and analyse the distribution using an optical microscope and ImageJ (Fiji distribution) in figure 1. Previous Raman measurements indicate similarities between dust produced in a carbon arc and in the National Spherical Torus eXperiment (NSTX) (Raitses *et al.* 2008).

Two models are used to describe the size distribution in figure 2, a power-law model and an exponential-law model,

$$n_d = n_0 (r/r_0)^{-\alpha} \tag{2.1}$$

and

$$n_d = n_0 \exp[-(r/r_0)^{\beta}]. \tag{2.2}$$

https://doi.org/10.1017/S0022377816000404 Published online by Cambridge University Press

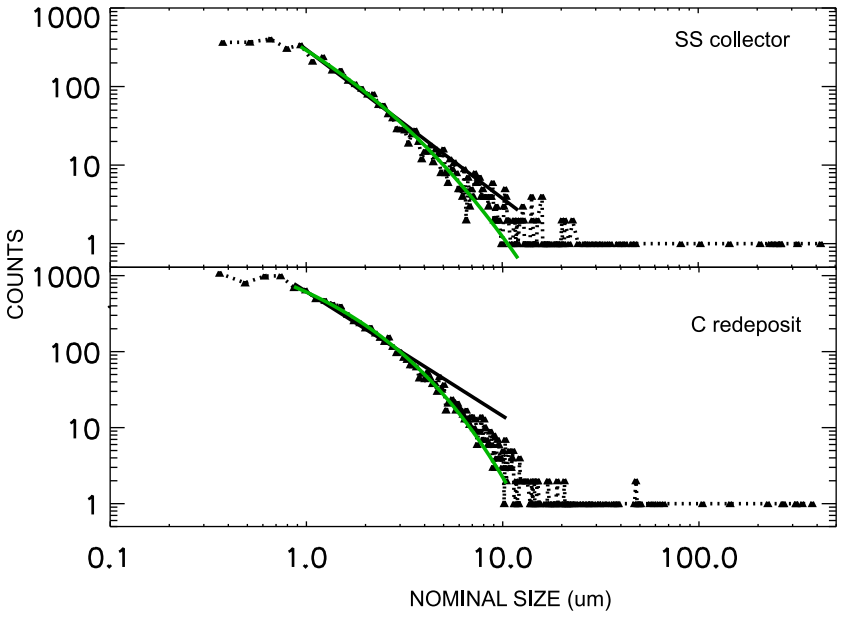

FIGURE 2. Dust-size distribution from a carbon-arc discharge. The number of dust particles increases rapidly as the size decreases, consistent with *in situ* measurements (Voinier *et al.* 2005).

For the stainless steel (SS) collector, the two models gives slightly different fits to the data. The fitting power in (2.1) is $\alpha = 1.89$. In the exponential model (2.2), $\beta = 0.331$. For the C-redeposit sample, the fitting power is $\alpha = 1.63$. The exponential model gives a better fit with $\beta = 0.564$.

2.2. *Dust velocities*

For dust with a small initial velocity ($\sim$ a few m s^{-1}), it can be accelerated by ion-drag forces in fusion plasmas at the edge as well as inside the edge pedestal. Due to ablation, the dust motion can be quite complicated (Pigarov *et al.* 2005; Wang *et al.* 2008; Bacharis *et al.* 2010; Krasheninnikov *et al.* 2011; Ratynskaia *et al.* 2013). We shall only estimate the magnitude of velocities for MPI development. When the dust velocity ($\boldsymbol{u}_d$) is small compared with plasma flow ($\boldsymbol{u}_i$), the force on the dust is approximately (Baines *et al.* 1965; Ticos *et al.* 2006*a*)

$$\boldsymbol{F} = 2\pi r_d^2 kT \sum_i n_i \frac{\boldsymbol{s}_i^3}{s_i}. \tag{2.3}$$

The sum is for different ion species. The normalized relative velocity $\boldsymbol{s}_i = (\boldsymbol{u}_i - \boldsymbol{u}_d)/v_i$ is the ion flow ($\boldsymbol{u}_i$) relative to the dust motion, with the normalization $v_i = \sqrt{2kT/m_i}$. It is interesting to estimate how fast dust can be accelerated by ion-drag force in fusion plasmas. For a constant ion drag and initial dust velocity $\boldsymbol{u}_d \sim 0$, (2.3) gives

$$s(t) = \frac{1}{\dfrac{t}{\tau_0} + \dfrac{1}{s_0}}, \tag{2.4}$$

https://doi.org/10.1017/S0022377816000404 Published online by Cambridge University Press

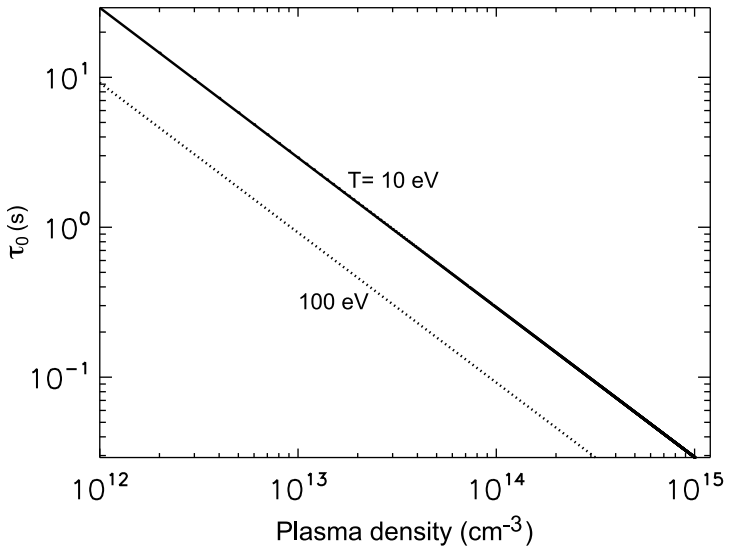

FIGURE 3. Entrain time τ_0 as a function of deuterium plasma density and temperature for carbon dust of 1 μm in radius. Dust granules are unlikely to approach plasma flow velocities in the km s^{-1} range.

where the characteristic time τ_0 is given by

$$\tau_0 = \frac{m_d v_i}{2\pi r_d^2 kTn}. \tag{2.5}$$

As expected, for the same dust size, higher density W particles take longer to be accelerated to the same speed than lower density particles of Be or C. τ_0 for fusion-relevant conditions is illustrated in figure 3 for carbon dust, which is in the hundreds of ms to tens of seconds range. Extrapolations to other materials and plasma conditions are possible using (2.5). When a dust grain moves for a distance L in the fusion plasma, it will reach a velocity u_d given by

$$u_d \sim \sqrt{\frac{2Lv_i}{\tau_0}}, \tag{2.6}$$

assuming the plasma flow is of the same order as the thermal velocity v_i. An example is shown in figure 4. Tens of m s^{-1} to hundreds of m s^{-1} is even possible depending on the dust mass and size.

3. Dust and micropellet destruction

A comprehensive model for dust and micropellet destruction due to evaporation and ablation in fusion plasmas is beyond the scope of this work. Numerical studies can be found for example in (Pigarov *et al.* 2005; Smirnov *et al.* 2007; Bacharis *et al.* 2010). Here we only discuss the simple case when the equations for dust or micropellet mass and transport are mutually independent. Dust or micropellets also move along straight-line trajectories at a constant velocity (u_d). The dust destruction depends on a single geometrical parameter (radius of the dust, r_d) and assumes

https://doi.org/10.1017/S0022377816000404 Published online by Cambridge University Press

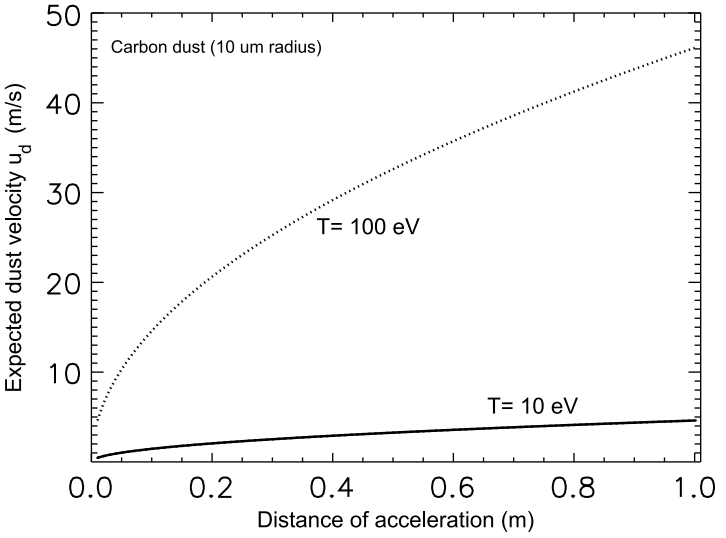

FIGURE 4. Expected dust velocity as a function of acceleration distance due to ion-drag force – carbon dust (10 μm in radius). The deuterium plasma density is $10^{19}\,\mathrm{m}^{-3}$.

spherical symmetry. We also assume single-temperature single-density (Maxwellian) distributions for plasma ions and electrons. The dust density is assumed to be low so that 'mutual shielding effects' are neglected. Experiments involving large pellets indicated that ablation is not spherically symmetric. The non-Maxwellian electron and ion distributions due to heating can enhance ablation significantly.

3.1. *Ablation model*

The ablation equation is

$$\frac{1}{M_0}\frac{\mathrm{d}m_d}{\mathrm{d}t} = -\frac{A_d \Gamma^{\infty} f_s}{E_0}, \tag{3.1}$$

which for a spherical micropellet may be rewritten as

$$\frac{\mathrm{d}r_d}{\mathrm{d}t} = -f_s c_a. \tag{3.2}$$

m_d, A_d, ρ_d and r_d are the dust or micropellet mass, surface area, mass density and radius, respectively. M_0 is the mass of individual atoms/molecules. E_0, the evaporation/sublimation energy per atom/molecule, is listed in table 2 for several materials. We introduce a characteristic ablation speed c_a that satisfies

$$c_a \equiv \frac{M_0}{\rho_0}\frac{\Gamma^{\infty}}{E_0}. \tag{3.3}$$

The heat flux at far away from the dust $\Gamma^{\infty} = \sum_j \Gamma_j^{\infty}$ is the sum of the thermal fluxes of electrons and ions. $\Gamma_j^{\infty} = n_j \bar{v}_j (2kT_j)/4$ and $\bar{v}_j = \sqrt{8kT_j/\pi m_j}$ with corresponding mass (m_j), temperature (T_j) and density (n_j) for ions and electrons, respectively. f_s is the heat flux shielding factor. If $0 < f_s < 1$, the heat flux is reduced due to ablation cloud shielding and dust charging and other secondary effects. If $f_s > 1$, the heat flux is enhanced due to dust–plasma interactions.

https://doi.org/10.1017/S0022377816000404 Published online by Cambridge University Press

Material	Density[a] (g cm^{-3})	E_0[b] (eV)	Evap. temp., T_0 (K)	Pre-ablation, E_1[c] (eV)
Li	0.512	1.41	1603	0.41
Be	1.69	3.03	3243	0.98
B	2.08	5.27	4200	1.66
C	2.27	6.28	3915[d]	0.94–1.53
W	17.6	8.02	6203	2.98–3.73

TABLE 2. Material properties for ablation models.

[a]Liquid density or solid density when sublimates.
[b]Based on evaporation/sublimation energy. For carbon, the value of 589 kJ mol^{-1} comes from Doehaerd *et al.* (1952).
[c]Per atom.
[d]Sublimation temperature.

3.2. *Pre-ablation phase*

As recognized in Kuteev *et al.* (1984), there is a pre-ablation phase for most non-cryogenic materials before evaporation and sublimation begin. We compiled a material property table based on Wikipedia and NIST condensed phase thermochemistry data (NIST 2016), shown in table 2. The pre-ablation energy per atom (E_1) is the mean energy that each atom will gain before evaporation or sublimation begins. Another way to estimate E_1 is to subtract the evaporation/sublimation energy (E_0) from the surface bonding energy of the atoms to the solid.

In the pre-ablation phase, $\mathrm{d}m_d/\mathrm{d}t \sim 0$. We may calculate the ability of dust and micropellets to penetrate through edge plasma and cross the separatrix as a function of size and velocity without losing any mass. We assume a constant plasma density of 10^{19} m^{-3} and temperature profiles $T_e(z) = T_i(z) = T_a + (T_b - T_a)z/z_0$, where $T_a = 10$ eV and $T_b = 200$ eV. $z = 0$ corresponds to the wall position. $z_0 = 10$ cm is the width of the SOL.

The electron and ion heating rates, Γ_e and Γ_i, can be related to the electron and ion currents (I_e and I_i) for Maxwellian distributions of electrons and ions,

$$\Gamma_e = -\frac{I_e}{e} 2kT_e, \quad \Gamma_i = \frac{I_i}{Z_i e} \frac{2kT_i - Z_i e\phi_d}{1 - Z_i e\phi_d/kT_i}, \tag{3.4a,b}$$

with $-I_e = I_i$, the vanishing current condition. The following assumptions are made: the sticking coefficients of electrons and ions on the dust are one, independent of their energies. The thermionic and secondary electron emissions, as well as radiative heating and cooling, are negligible. The vanishing current condition is used to find ϕ_d self-consistently through

$$\bar{v}_e \exp\frac{e\phi_d}{kT_e} = \bar{v}_i \left(1 - \frac{Z_i e\phi_d}{kT_i}\right). \tag{3.5}$$

For $T_i = T_e = T$ and $Z_i = 1$ (hydrogen and deuterium plasmas), the ratio $e\phi_d/kT$ is independent of T and has the value of –2.504 and –2.776 for hydrogen and deuterium plasma, respectively.

For an SOL of width L_0, the dust penetration without evaporation gives the minimum dust velocity required before ablation starts,

$$u_d^{min} = \int_0^{L_0} \mathrm{d}z \frac{\Gamma_e + \Gamma_i}{N_d E_1}, \tag{3.6}$$

https://doi.org/10.1017/S0022377816000404 Published online by Cambridge University Press

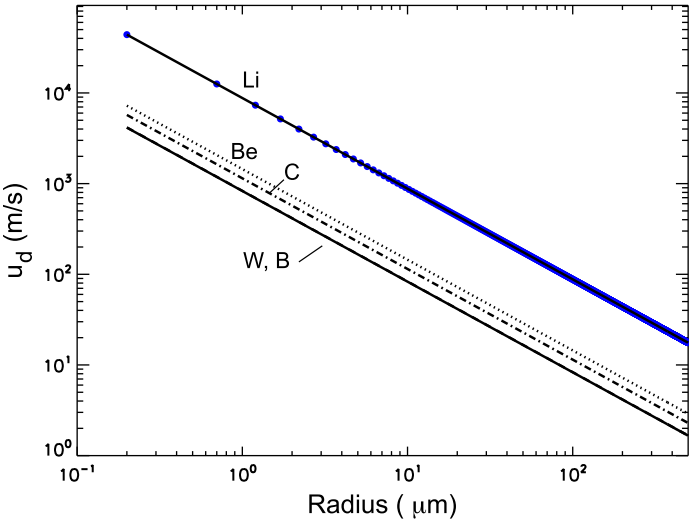

FIGURE 5. Minimum dust velocity required to penetrate a 'model' edge plasma with a constant density of 10^{19} m^{-3} and a linear variation of temperature from 10 to 200 eV. The same pre-ablation model can be applied to other realistic edge-plasma scenarios.

where the integration is along the trajectory of the dust. N_d is the initial number of atoms/molecules contained in the dust and E_1 is given in table 2. u_d^{min} for several materials are shown in figure 5.

3.3. *The shielding factor f_s and surface neutral density n_{surf}*

In the 'small' or orbital motion limit (OML), the shielding factor f_s for Maxwellian distributions ($T_i = T_e = T$) can also be calculated as

$$f_s = \frac{\Gamma_e + \Gamma_i}{\Gamma^\infty} = \frac{\bar{v}_e}{\bar{v}_e + \bar{v}_i} \exp\left(\frac{e\phi_d}{kT}\right) + \frac{\bar{v}_i}{\bar{v}_e + \bar{v}_i}\left(1 - \frac{e\phi_d}{2kT}\right). \tag{3.7}$$

The temperature dependence cancels out for $T_i = T_e = T$, which yields $f_s = 0.134$ and 0.102 for hydrogen and deuterium plasmas and the self-consistent $e\phi_d$ as given above. f_s as a function of $e\phi_d$ is shown in figure 6.

For sufficiently large dust, $f_s < 1$ due to the shielding of the ablation cloud, which consists of neutral atoms and so-called 'secondary' plasma. Ionization of the neutral atoms gives rise to the secondary plasma, to distinguish it from the surrounding plasma or the 'primary' plasma. The shielding of the cloud is not effective when the condition

$$\int_{r_d}^{\infty} \mathrm{d}r n_0(r, r_d) M_0 \leqslant \rho_0 R_e \tag{3.8}$$

is met. The left-hand side is the areal density of the neutral-atom cloud. R_e on the right-hand side is the electron range in the cloud corresponding to a density ρ_0. The product $\rho_0 R_e$ is a material property. The neutral density $n_0(r, r_d)$ is given by

$$n_0(r, r_d) = n_{surf}(r_d') \exp\left(-\frac{r - r_d'}{\Lambda_e}\right), \tag{3.9}$$

https://doi.org/10.1017/S0022377816000404 Published online by Cambridge University Press

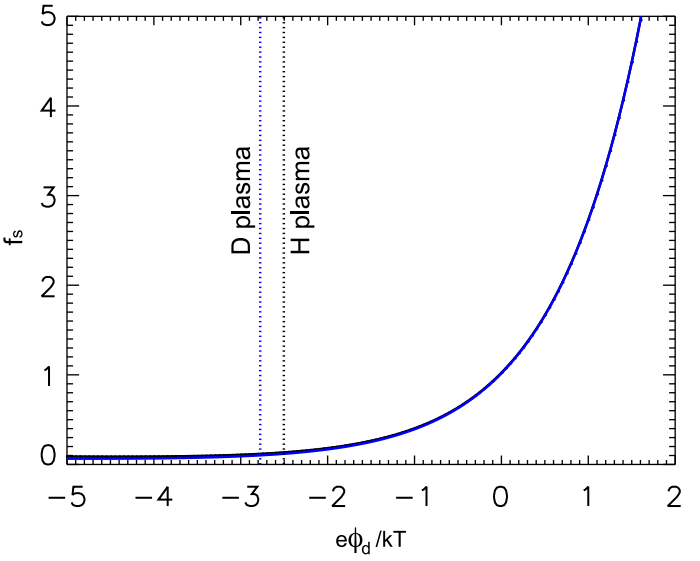

FIGURE 6. Shielding factor (f_s) as a function of dust potential ϕ_d (normalized to plasma temperature T).

where $\Lambda_e = u_0/(n_e\langle\sigma_{i0}v_e\rangle)$ is the neutral ionization mean free path, n_e the electron density and $\langle\sigma_i v_e\rangle$ the average ionization rate coefficient. u_0 is the speed of the neutrals leaving the dust surface and it remains constant until they collide with another atom or heavy ion. Electrons are too light to deflect the neutrals. Here we introduce a new variable $n_{surf}(r_d)$, which is the surface neutral density when the dust is at radius r_d. r_d' is related to the instantaneous radius r_d through a time delay δt as

$$\delta t = \frac{r - r_d'}{u_0} = \int_{r_d}^{r_d'} \mathrm{d}s \frac{1}{f_s c_a} \tag{3.10}$$

based on the ablation (3.2) and (3.3) for c_a. Assuming that f_s remains constant for the period when the dust or micropellet shrinks from a size r_d' to r_d, solution of equation (3.10) for r_d' gives

$$r_d' = \frac{f_s c_a r + u_0 r_d}{u_0 + f_s c_a}, \quad r \geqslant r_d. \tag{3.11}$$

From neutral particle flux conservation, the surface density $n_{surf}(r_d)$ is given by

$$n_{surf}(r_d) = \frac{\Gamma^{\infty} f_s}{E_0 u_0} = \frac{\rho_0}{M_0}\frac{f_s c_a}{u_0}. \tag{3.12}$$

The neutral atoms expand thermally at the evaporation temperature with a radial velocity of up to $u_0 = \sqrt{2kT_0/3M_0}$. Here the factor 3 takes into account that the total thermal energy kT_0 from evaporation is equally shared among the three degrees of freedom. The transition radius as a function of $n_{surf}(r_d)$ has been calculated for Li and C in figure 7.

https://doi.org/10.1017/S0022377816000404 Published online by Cambridge University Press

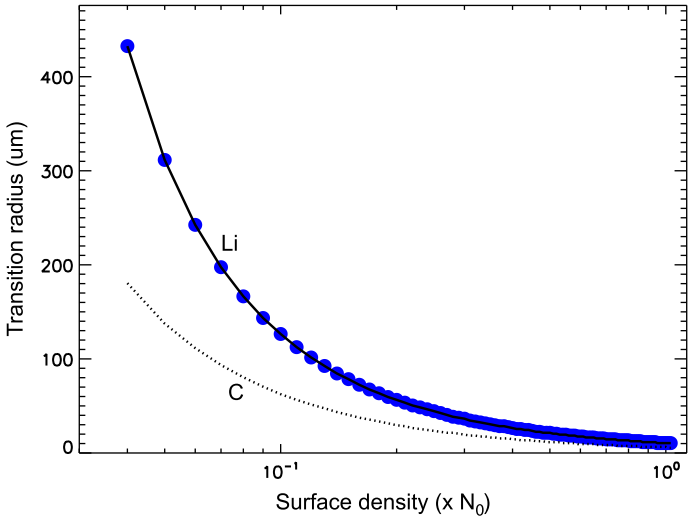

FIGURE 7. Transition dust radius as a function of the surface neutral density (n_{surf}) for Li and C spheres. $N_0 = 2.69 \times 10^{19}\,\mathrm{m}^{-3}$ (the ideal gas density at STP). The plasma is assumed to be at 100 eV with a density of 10^{19} m^{-3}.

4. Stopping of energetic particles

Energetic ions in magnetic fusion plasmas come from fusion reaction as well as ion heating. Energetic electrons come from heating and runaway processes. Runaway electrons (REs) are generated through Dreicer acceleration and avalanche (multiplication) (Rosenbluth & Putvinski 1997). We can compare the ion stopping and energetic electron stopping in materials. Figure 8 shows the energetic ion (p and α) ranges in different materials using SRIM. The results show that energetic ions expected in magnetic fusion can be readily stopped by individual micropellets in 10–100 μm, while REs will take at least hundreds of micropellets with a medium atomic number (Z_m), as shown in figure 9.

5. Experimental aspects of MPI

Application of hypervelocity dust injection to high-temperature plasma diagnostics was discussed previously (Wang & Wurden 2003, 2004; Wang *et al.* 2007; Ticos *et al.* 2008). The latest progress in using pellets of different sizes and materials for ELM pacing and the proposed shattered pellet injection (SPI) for ITER disruption mitigation (Baylor *et al.* 2009) indicate broader roles for high-speed (>0.5 km s^{-1}) micropellet injection to control the transient heat flux and possibly to provide stellarator core fuelling. In addition to injection speed, the abilities to cover a wider range of mass-injection rates, frequencies and material choices are areas of interest (Loarte *et al.* 2014). Mass-injection methods are currently developed in parallel with externally applied non-axisymmetric or 'three-dimensional' magnetic perturbations (Schaffer *et al.* 2008; Canik *et al.* 2010).

5.1. *Granule dropper experiments in NSTX*

A compact piezoelectrically actuated granule dropper has enabled several successful injections of both low-Z (Li) and high-Z (W) dust into tokamaks (Mansfield *et al.*

https://doi.org/10.1017/S0022377816000404 Published online by Cambridge University Press

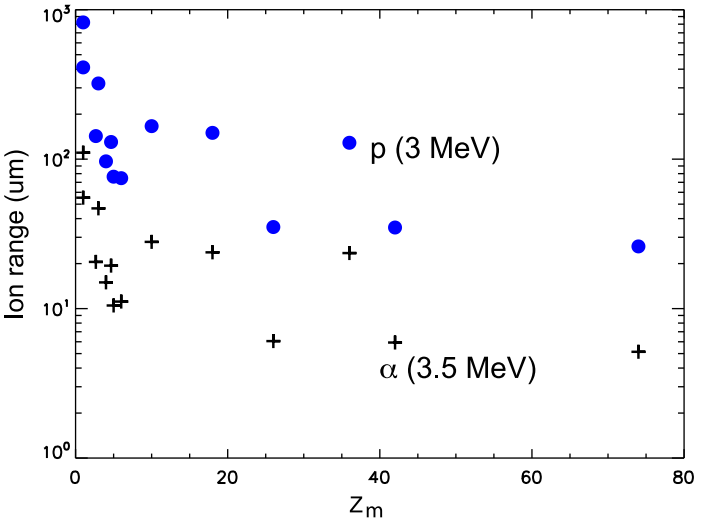

FIGURE 8. SRIM predictions of energetic ion (3 MeV p and 3.5 MeV α) stopping in matter. The results indicate that individual dust grains of the order of 100 μm in radius are sufficient to stop MeV ions.

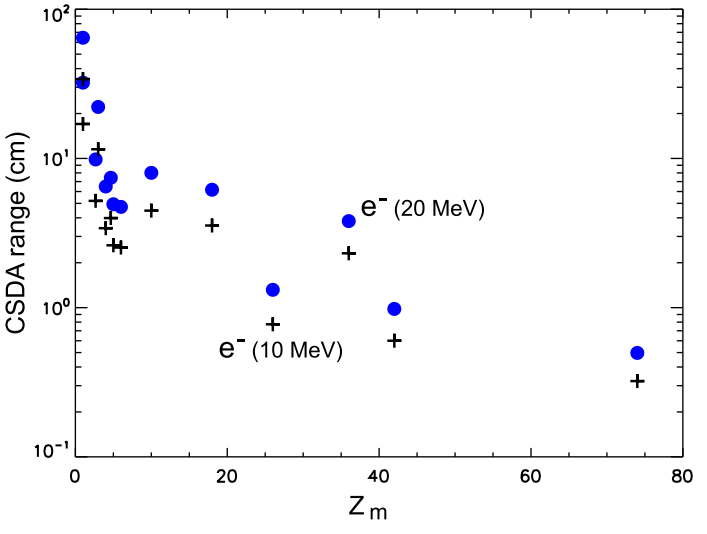

FIGURE 9. Continuous slowing down approximation (CSDA) ranges of energetic electrons in matter. The results indicate that individual dust grains are not sufficient to stop 10–20 MeV electrons, which are expected during ITER-like disruptions. A thick cloud with equivalent matter thickness of the order of 1–10 cm would be needed for medium-Z materials.

2013). By varying the amplitude of the piezoelectric oscillation at a resonance around 2 kHz, the dropper provided a regulated mass injection which was rapidly aerosolized as it impacted the edge plasma. Commercial spherical Li powder with a 44 μm average diameter was stabilized against reaction with air by a 30 nm thick mantle of Li_2CO_3. When dust particles were gravitationally accelerated, their velocities were

https://doi.org/10.1017/S0022377816000404 Published online by Cambridge University Press

around 3 m s^{-1}. When used in conjunction with a mechanical propeller, granule velocities of up to tens of m s^{-1} have been achieved. In long-pulse tokamaks, the dust dropper has shown the ability to reliably provide real-time Li injection rates between 1 and 120 mg s^{-1} for periods of up to 30 s (Hu *et al.* 2014).

The three-dimensional motion of lithium dust in NSTX was tracked using two toroidally separated fast visible cameras (Nichols *et al.* 2011). Between 10 and 250 mg of Li dust were dropped into H-mode discharges with neutral beam heating power of 2–6 MW, plasma current (I_p) 0.9 MA and discharge duration 1.0–1.3 s. While a statistically representative sample could not be obtained, it was clear that most (∼90 %) dust particles drifted perpendicular to field lines, while a smaller (∼10 %) population accelerated along field lines and an even smaller (<1 %) population changed direction mid-flight. Even at the highest injection rates, no Li dust particles were observed to cross the separatrix. Additionally, no discharges were lost to disruptions due to the injection of Li dust, and in some cases the introduction of Li dust improved confinement.

In the case of W injection, an approximate rate of 3 mg s^{-1} was achieved for the duration of a 700 ms NSTX discharge (Clementson *et al.* 2010). In that case, the W particles took the form of irregularly shaped crystals with 5 μm average diameter and maximum dimension of 10 μm. W dust trajectories were also obtained, but they are not directly comparable to Li trajectories because NSTX was operating with a reversed toroidal field at the time. Significant W radiation was observed in the core during the dust injection, and W dust appeared to have crossed the separatrix, but nevertheless the discharge did not disrupt. Furthermore, during the subsequent discharges with no W injection, there was no spectroscopic evidence of W residue in the core, indicating that injected W particles had been pumped away or deposited on a plasma-facing component (PFC) surface.

5.2. *MPI technologies*

In addition to gas injection and pellet injectors based on high-pressure gas acceleration, several mass-injection technologies are shown in figure 10 in the velocity versus radius plot. The velocity scales with radius as $u_d \propto r_d^{-1}$ because of the fact that the forces of acceleration are proportional to r_d^2 while the mass scales with radius as $m_d \propto r_d^3$. In comparison with fuelling pellets moving at several hundred m s^{-1}, higher speeds and smaller masses can be advantageous for many applications (Plöckl *et al.* 2011). Blower guns, centrifuge launchers (IPP 0000) and rail guns are some other possibilities for larger mass. Supersonic molecular beam injectors are examples for smaller mass (Xiao *et al.* 2012).

5.3. *Materials of interest*

For PMI research, it is useful to examine dust transport of carbon, Be, W and compounds of these first wall/divertor materials. For ELM pacing and disruption mitigation, additional low-Z (Li and LiD for example) and high-Z materials should be examined. Material selection is also constrained by availability, safety (fire hazard and health hazard) and the method of injection.

Recent induced ELM pacing experiments with conventional cryogenic pellets in DIII-D as well as room-temperature lithium granule injection in EAST (Wu 2007) have motivated further ELM pacing studies (Baylor *et al.* 2013; Mansfield *et al.* 2013). In NSTX-U (U for 'upgrade' that just finished recently), for example, both boron carbide splinter powder and vitreous carbon microspheres have undergone

https://doi.org/10.1017/S0022377816000404 Published online by Cambridge University Press

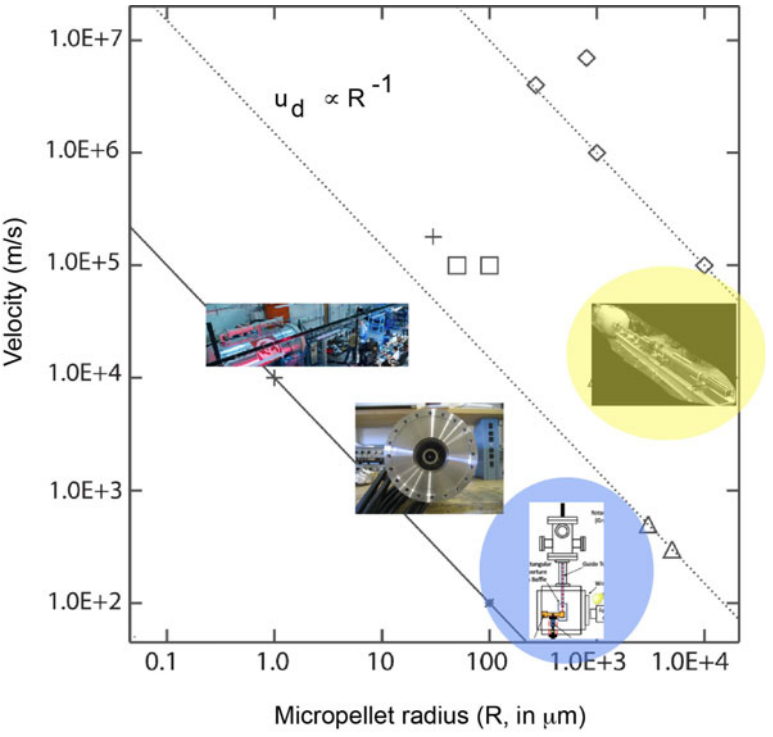

FIGURE 10. A comparison of different mass-injection technologies. Along the lowest slanted line from the top to the bottom are an electrostatic dust accelerator (Shu *et al.* 2012), a plasma-drag accelerator (Ticos *et al.* 2006*b*) and a mechanical lithium propeller (Mansfield *et al.* 2013). Along the slanted line above is a two-stage gas gun (Physics Applications Inc. 0000). No technology exists today along the top slanted line.

laboratory testing in preparation for the upcoming run campaign. Both granule types were impurity assayed by Evans Analytical Group (EAG) utilizing glow-discharge mass spectroscopy. While the carbon microspheres were found to be of high purity (99.9 %+) the boron carbide splinter powders were found to contain fractional percentages of the impurities Si and Fe at the 0.57 % and 0.15 % levels, respectively. The carbon and boron carbide granules have been grouped into three average sizes of 300, 600 and 900 μm. It is anticipated that 50–100 Hz injection of these microgranules into the edge of NSTX-U plasmas will accelerate the frequency of ELMs and thereby reduce the peak heat load to the divertor.

5.4. *Possible new experiments*

Extensive laboratory experiments will be needed to develop MPI technologies for various applications. Major fusion experiments such as NSTX-U, DIII-D, JET, W7-X (Beidler *et al.* 1990), EAST and others can be complemented by smaller scale laboratory experiments, which allow better access for systematic examination of MPI physics and technology. Several facilities in the USA, shown in table 3, are used as illustrations here. The Hybrid Illinois Device for Research and Applications (HIDRA) facility (Andruczyk *et al.* 2015) allows dust transport and ablation research. The

https://doi.org/10.1017/S0022377816000404 Published online by Cambridge University Press

Facility	Geometry	Density (m^{-3})	Magnetic field (T)	Hot ions (eV)
HIDRA	Toroidal	10^{17}–10^{18}	0.5	$\leqslant$200
MDPX	Cylindrical	10^{15}–10^{16}	$>$3	$<$1
MPEX	Linear	10^{19}–10^{21}	1	$\leqslant$20
NSTX-U	Toroidal	10^{19}–10^{20}	1	$>10^{3}$

TABLE 3. Possible facilities for new micropellet injection experiments and development.

Magnetized Dusty Plasma eXperiment (MDPX) (Thomas *et al.* 2015) permits dust charging at elevated temperatures and dust generation. The Material Plasma Exposure eXperiment (MPEX) (Rapp *et al.* 2013) allows examination of dust dynamics and erosions in divertor-like conditions.

6. Conclusion

Plasma–material interactions in the ITER era give rise to new challenges and opportunities for micropellet injection (MPI) technology, extending its existing usages as a tool to understand dust dynamics and plasma diagnostics in magnetic fusion. A variety of MPI technologies that differ in the amount of mass delivery, material type (Z), injection velocity and injection frequency can find applications in heat mitigation (ELM pacing and disruption mitigation, for example), energetic particle mitigation, plasma diagnostics, dust studies and fuelling. New experimental facilities such as MDPX, HIDRA and MPEX complement the major fusion experiments for MPI development.

REFERENCES

ANDRUCZYK, D., RUZIC, D. N., ALLAIN, J. P. & CURRELI, D. 2015 HIDRA: Hybrid Illinois device for research and applications. *Fusion Sci. Technol.* **68**, 497–500.

BACHARIS, M., COPPINS, M. & ALLEN, J. E. 2010 Dust in tokamaks: an overview of the physical model of the dust in tokamaks code. *Phys. Plasmas* **17**, 042505, 1–11.

BAINES, M. J., WILLIAMS, I. P. & ASEBIOMO, A. S. 1965 Resistance to the motion of a small sphere moving through a gas. *Mon. Not. R. Astron. Soc.* **130**, 63–74.

BAYLOR, L. R., COMBS, S. K., FOUST, C. R., JERNIGAN, T. C., MEITNER, S. J., PARKS, P. B., CAUGHMAN, J. B., MARUYAMA, S., QUALLS, A. L., RASMUSSEN, D. A. *et al.* 2009 Pellet fueling, ELM pacing, and disruption mitigation technology development for ITER. *Nucl. Fusion* **49**, 085013, 1–8.

BAYLOR, L. R., COMMAUX, N., JERNIGAN, T. C., BROOKS, N. H., COMBS, S. K., EVANS, T. E., FENSTERMACHER, M. E., ISLER, R. C., LASNIER, C. J., MEITNER, S. J. *et al.* 2013 Reduction of edge-localized mode intensity using high-repetition-rate pellet injection in tokamak H-mode plasmas. *Phys. Rev. Lett.* **110**, 245001, 1–5.

BEHRISCH, R. 1991 Particle bombardment and energy fluxes to the vessel walls in controlled thermonuclear fusion devices. In *Atomic and Plasma–Material Interaction Data for Fusion*, vol. 1, pp. 7–16. IAEA.

BEIDLER, C., GRIEGER, G., HERRNEGGER, F., HARMEYER, E., KISSLINGER, J., LOTZ, W., MAASSBERG, H., MERKEL, P., NUHRENBERG, J., RAU, F. *et al.* 1990 Physics and engineering design for W7-X. *Fusion Technol.* **17**, 148.

https://doi.org/10.1017/S0022377816000404 Published online by Cambridge University Press

BROOKS, J. N. 2002 Modeling of sputtering erosion/redeposition – status and implications for fusion design. *Fusion Engng Des.* **60**, 515–526.

CANIK, J. M., MAINGI, R., EVANS, T. E., BELL, R. E., GERHARDT, S. P., KUGEL, H. W., LEBLANC, B. P., MANICKAM, J., MENARD, J. E., OSBORNE, T. H. *et al.* 2010 ELM destabilization by externally applied non-axisymmetric magnetic perturbations in NSTX. *Nucl. Fusion* **50**, 034012, 1–8.

CLEMENTSON, J., BEIERSDORFER, P., ROQUEMORE, A. L., SKINNER, C. H., MANSFIELD, D. K., HARTZFELD, K. & LEPSON, J. K. 2010 Experimental setup for tungsten transport studies at the NSTX tokamak. *Rev. Sci. Instrum.* **81**, 10E326, 1–3.

DOEHAERD, TH., GOLDFINGER, P. & WAELBROECK, F. 1952 Direct determination of the sublimation energy of carbon. *J. Chem. Phys.* **20**, 757.

FEDERICI, G., SKINNER, C. H., BROOKS, J. N., COAD, J. P., GRISOLIA, C., HAASZ, A. A., HASSANEIN, A., PHILIPPS, V., PITCHER, C. S., ROTH, J. *et al.* 2001 Plasma–material interactions in current tokamaks and their implications for next step fusion reactors. *Nucl. Fusion* **41** (12R), 1967–2137.

HU, J. S., REN, J., SUN, Z., ZUO, G. Z., YANG, Q. X., LI, J. G., MANSFIELD, D. K., ZAKHAROV, L. E. & RUZIC, D. N. 2014 An overview of lithium experiments on HT-7 and EAST during 2012. *Fusion Engng Des.* **89**, 2878–2885.

IPP http://www.ipp.mpg.de/1124592/gun (last accessed 2015).

KRASHENINNIKOV, S. I., SMIRNOV, R. D. & RUDAKOV, D. L. 2011 Dust in magnetic fusion devices. *Plasma Phys. Control. Fusion* **53**, 083001, 1–54.

KUTEEV, B. V., SERGEEV, V. Y. & TSENDIN, L. D. 1984 Two-dimensional kinetic model for the evaporation of hydrogen pellets in a tokamak. *Sov. J. Plasma Phys.* **10** (6), 675–679.

LANG, P. T., CONWAY, G. D., EICH, T., GRUBER, L., GÜNTER, O., HORTON, S., KALLENBACH, L. D., KAUFMANN, S., LORENZ, A., MARASCHEK, M. *et al.* 2004 ELM pace making and mitigation by pellet injection in ASDEX upgrade. *Nucl. Fusion* **44**, 665–677.

LANG, P. T., LOARTE, A., SAIBENE, G., BAYLOR, L. R., BECOULET, M., CAVINATO, M., CLEMENT-LORENZO, S., DALY, E., EVANS, T. E., FENSTERMACHER, M. E. *et al.* 2013 ELM control strategies and tools: status and potential for ITER. *Nucl. Fusion* **53**, 043004, 1–24.

LEONARD, A. W., HERRMANN, A., ITAMI, K., LINGERTAT, J., LOARTE, A., OSBORNE, T. H. & SUTTROP, W. 1999 The impact of ELMs on the ITER divertor. *J. Nucl. Mater.* **266–269**, 109–117.

LOARTE, A., HUIJSMANS, G., FUTATANI, S., BAYLOR, L. R., EVANS, T. E., ORLOV, D. M., SCHMITZ, O., BECOULET, M., CAHYNA, P., GRIBOV, Y. *et al.* 2014 Progress on the application of ELM control schemes to ITER scenarios from the non-active phase to DT operation. *Nucl. Fusion* **54**, 033007, 1–18.

MANSFIELD, D. K., ROQUEMORE, A. L., CARROLL, T., SUN, Z., HU, J. S., ZHANG, L., LIANG, Y. F., GONG, X. Z., LI, J. G., GUO, H. Y. *et al.* 2013 First observations of ELM triggering by injected lithium granules in EAST. *Nucl. Fusion* **53**, 113023, 1–7.

NICHOLS, J., ROQUEMORE, A. L., DAVIS, W., MANSFIELD, D. K., SKINNER, C. H., FEIBUSH, E., BOEGLIN, W., PATEL, R., ABOLAFIA, D., HARTZFELD, K. *et al.* 2011 3-D reconstruction of pre-characterized lithium and tungsten dust particle trajectories in NSTX. *J. Nucl. Mater.* **415**, S1098–S1101.

NIST 2016 http://webbook.nist.gov.

Physics Applications Inc. http://www.physicsapp.com/two-stage_gas_guns.html (last accessed 2015).

PIGAROV, A. Y., KRASHENINNIKOV, S. I., SOBOLEVA, T. K. & ROGNLIEN, T. D. 2005 Dust-particle transport in tokamak edge plasmas. *Phys. Plasmas* **12**, 122508, 1–15.

PITTS, R. A., CARPENTIER, S., ESCOURBIAC, F., HIRAI, T., KOMAROV, V., LISGO, S., KUKUSHKIN, A. S., LOARTE, A., MEROLA, M., SASHALA NAIK, A. *et al.* 2013 A full tungsten divertor for ITER: physics issues and design status. *J. Nucl. Mater.* **438**, S48–S56.

https://doi.org/10.1017/S0022377816000404 Published online by Cambridge University Press

PLÖCKL, B., LANG, P. T., JEHL, J., PRECHTL, M. & SOTIER, S. 2011 Comparison of different pellet injection systems for ELM pacing. *Fusion Engng Des.* **86**, 1022–1025.

RAITSES, Y., SKINNER, C. H., JIANG, F. & DUFFY, T. S. 2008 Raman spectroscopy of carbon dust samples from NSTX. *J. Nucl. Mater.* **375**, 365–369.

RAPP, J., BIEWER, T. M., CANIK, J., CAUGHMAN, J. B. O., GOULDING, R. H., HILLIS, D. L., LORE, J. D. & OWEN, L. W. 2013 The development of plasma–material interaction facilities for the future of fusion technology. *Fusion Sci. Technol.* **64**, 237–244.

RATYNSKAIA, S., VIGNITCHOUK, L., TOLIAS, P., BYKOV, I., BERGSKER, H., LITNOVSKY, A., DEN HARDER, N. & LAZZARO, E. 2013 Migration of tungsten dust in tokamaks: role of dust–wall collisions. *Nucl. Fusion* **53**, 123002, 1–10.

ROSENBLUTH, M. N. & PUTVINSKI, S. V. 1997 Theory for avalanche of runaway electrons in tokamaks. *Nucl. Fusion* **37** (10), 1355–1362.

SCHAFFER, M. J., MENARD, J. E., ALDAN, M. P., BIALEK, J. M., EVANS, T. E. & MOYER, R. A. 2008 Study of in-vessel nonaxisymmetric ELM suppression coil concepts for ITER. *Nucl. Fusion* **48**, 024004, 1–14.

SHU, A., COLLETTE, A., DRAKE, K., GRÜN, E., HORÁNYI, M., KEMPF, S., MOCKER, A., MUNSAT, T., NORTHWAY, P., SRAMA, R. *et al.* 2012 3 MV hypervelocity dust accelerator at the Colorado center for lunar dust and atmospheric studies. *Rev. Sci. Instrum.* **83** (7), 075108, 1–8.

SMIRNOV, R. D., PIGAROV, A. YU., ROSENBERG, M., KRASHENINNIKOV, S. I. & MENDIS, D. A. 2007 Modelling of dynamics and transport of carbon dust particles in tokamaks. *Plasma Phys. Control. Fusion* **49**, 347–371.

THOMAS, E., KONOPKA, U., ARTIS, D., LYNCH, B., LEBLANC, S., ADAMS, S., MERLINO, R. L. & ROSENBERG, M. 2015 The magnetized dusty plasma experiment (MDPX). *J. Plasma Phys.* **81**, 345810206, 1–21.

TICOS, C. M., WANG, Z., DELZANNO, G. L. & LAPENTA, G. 2006*a* Plasma dragged microparticles as a method to measure plasma flows. *Phys. Plasmas* **13**, 103501, 1–10.

TICOS, C. M., WANG, Z., DORF, L. A. & WURDEN, G. A. 2006*b* Plasmadynamic hypervelocity dust injector for the National Spherical Torus Experiment. *Rev. Sci. Instrum.* **77**, 10E304, 1–3.

TICOS, C. M., WANG, Z., WURDEN, G. A., KLINE, J. L., MONTGOMERY, D. S. & DORF, L. A. 2008 Experimental demonstration of plasma-drag acceleration of a dust cloud to hypervelocities. *Phys. Rev. Lett.* **100**, 155002, 1–4.

VOINIER, C., SKINNER, C. & ROQUEMORE, A. 2005 Electrostatic dust detection on remote surfaces. *J. Nucl. Mater.* **346**, 266–271.

WANG, Z., SKINNER, C. H., DELZANNO, G. L., KRASHENINNIKOV, S. I., LAPENTA, G. M., PIGAROV, A. YU., SHUKLA, P. K., SMIRNOV, R. D., TICOS, C. M. & WEST, W. P. 2008 Physics of dust in magnetic fusion devices. In *New Aspects of Plasma Physics, Proceedings of the ICTP Summer College on Plasma Physics*, pp. 394–475. World Scientific.

WANG, Z., TICOS, C. M. & WURDEN, G. A. 2007 Dust trajectories and diagnostic applications beyond strongly coupled dusty plasmas. *Phys. Plasmas* **14**, 103701, 1–11.

WANG, Z. & WURDEN, G. A. 2003 Hypervelocity dust beam injection for internal magnetic field mapping. *Rev. Sci. Instrum.* **74**, 1887–1891.

WANG, Z. & WURDEN, G. A. 2004 Hypervelocity dust beam injection for national spherical torus experiment. *Rev. Sci. Instrum.* **75**, 3436–3438.

WU, S. 2007 An overview of the EAST project. *Fusion Engng Des.* **82**, 463–471.

XIAO, W. W., DIAMOND, P. H., KIM, W. C., YAO, L. H., YOON, S. W., DING, X. T., HAHN, S. H., KIM, J., XU, M., CHEN, C. Y. *et al.* 2012 ELM mitigation by supersonic molecular beam injection: KSTAR and HL-2A experiments and theory. *Nucl. Fusion* **52**, 114027, 1–8.